



A simple three-dimensional model of thermo–chemical convection in the mantle wedge

Satoru Honda ^{a,*}, Taras Gerya ^b, Guizhi Zhu ^b

^a Earthquake Research Institute, University of Tokyo, 1-1-1 Yayoi, Bunkyo-ku, Tokyo 113-0032, Japan

^b Institute of Geophysics, Swiss Federal Institute of Technology (ETH, Zurich), CH-8092, Switzerland

ARTICLE INFO

Article history:

Received 16 August 2009

Received in revised form 9 October 2009

Accepted 11 December 2009

Available online 18 January 2010

Editor: Y. Ricard

Keywords:

thermo–chemical convection

mantle wedge

subduction zones

ABSTRACT

In order to understand the possible existence of small-scale convection in the mantle wedge, we have constructed a simple three-dimensional model of convection driven by both thermal and chemical buoyancies above the subducting slab. In this model, a chemical agent, which affects both the density and the viscosity of mantle, is introduced from the top of the subducting slab and the associated density and viscosity decreases are treated as parameters. The model does not include the along-arc variation of the source of the chemical agent. We found that the major effects of low density chemical anomaly are to suppress the three-dimensional instability and make the flow two-dimensional, i.e., the flow velocity is normal to the plate boundary. The chemically polluted region tends to stay in the corner of the mantle wedge because of its low density and this results in the low temperature zone there. This suggests the importance of chemical buoyancy on the origin of cold mantle part or “nose” in the corner of the mantle wedge. We also studied the hybrid case: The region closer to the trench is in the low density and viscosity state and the region in the back arc is in the low viscosity state only. This case shows the existence of the low temperature nose and the small-scale thermally driven convection in the back arc. We also investigated the nature of the flip-flop phenomenon of the thermally driven convection and found that the thickness of the thermal boundary layer under the back arc controls it. This flow pattern in the back arc may have a close connection with the temporal and spatial variation of volcano distribution.

© 2009 Elsevier B.V. All rights reserved.

1. Introduction

Arc volcanisms and the subduction of slabs under the arcs are one of the most prominent features of the near-surface tectonics. Despite this, the details of mechanisms associated with these phenomena are still in much controversy.

Early studies of the subduction zone attributed the origin of arc volcanisms to the shear heating caused by the relative motion between the subducting slab and the overlying mantle (e.g., Hasebe et al., 1970; Toksoz et al., 1971). However, this view was questioned because of relatively high shear stress (a few kilobars) required for the melting of the mantle material. Later evolution of theory concerned with the role played by the water released from the subducting slab. Since it will lower the melting point of mantle rock, we may not require high viscous dissipation for melting. Besides this, the water or fluid plays other important role on the dynamics of mantle wedge, that is, it will make the viscosity and the density of the mantle low (e.g., Karato and Wu, 2003; Gerya and Yuen, 2003a). Thus the mantle wedge dynamics is controlled both by the rheology and density

affected by both thermal and chemical origins. Although the researchers noticed this importance of fluid phase, it is quite difficult to incorporate such effects in the model. This is mainly because we do not know the mechanism of transportation of such fluid in the mantle wedge, while the phase relation, which determines the estimate of fluid phase is well investigated (e.g., Poli and Schmidt, 2002).

Despite such difficulties, many workers have been trying to include such effects in the subduction zone models. For example, Iwamori (1998) considered the thermal aspects of the transportation of water and Gerya et al. (2002, 2004) and Arcay et al. (2005) considered the viscosity change associated with the presence of water. Recently, Gerya and his co-workers have developed more complicated model of subduction zone (Gerya et al., 2006; Nikolaeva et al., 2008). Their most recent model is a 3D model and the complexity arisen from the rock types and water is implemented by the particle approach (Zhu et al., 2009). Their results show a variety of dynamical behavior of the mantle wedge such as the formation of finger-like, wave-like and ridge-like plumes.

Since there are many and possibly uncertain parameters involved in this problem, the interpretation of the results of a complex model sometimes encounters difficulties. Considering this, we have constructed a simple model to understand the basic characteristics of mantle flow in the mantle wedge. Special attention is paid to the

* Corresponding author. Tel.: +81 3 5841 5725; fax: +81 3 5802 3391.

E-mail addresses: honda@eri.u-tokyo.ac.jp (S. Honda), taras.gerya@erdw.ethz.ch (T. Gerya), guizhi.zhu@erdw.ethz.ch (G. Zhu).

relation between the thermal and chemical buoyancy. The chemical effects are taken into account by parametrizing the transport velocity of fluid and the reductions of viscosity and density. We hope that present results may help understanding the results of complex and realistic models of subduction zone and eventually the arc volcanism.

2. Model and method

We assume that the mantle is incompressible viscous fluid with the Boussinesq approximation applied. The inertia term is neglected because of high viscosity. Newtonian viscosity is assumed to simplify the problem and to understand the results easily. Under these assumptions, the basic equations describing the mantle behavior in the Cartesian frame may be written as follows:

Conservation of mass:

$$\nabla \cdot \underline{v} = 0 \quad (1)$$

Conservation of linear momentum:

$$\nabla \cdot \underline{\tau} - \nabla p = \rho g \underline{e}_z \quad (2)$$

Constitutive relation:

$$\tau_{ij} = \eta(v_{ij} + v_{ji}) \quad (3)$$

Conservation of energy:

$$\frac{\partial T}{\partial t} + \underline{v} \cdot \nabla T = \kappa \nabla^2 T \quad (4)$$

Equation of state:

$$\rho = \rho_0(1 - \alpha T) - \Delta\rho_c \quad (5)$$

where \underline{v} is the velocity, τ (τ_{ij} ; $i, j = x, y, z$) is the stress tensor, p is the pressure, ρ is the density, g is the gravity, η is the viscosity, T is the temperature, \underline{e}_z is the unit vertical vector (positive upward), t is the time, κ is the thermal diffusivity, ρ_0 is the reference density, α is the coefficient of thermal expansion, $\Delta\rho_c$ is the density difference caused by the pollution of chemical agent and c is its concentration ($0 \leq c \leq 1$).

Besides these equations, we need the equation describing the concentration of the chemical agent, i.e., c . Since, we implicitly assume that such a chemical agent is water, we took the approach adopted by Gerya and his co-workers (Gorczyk et al., 2007; Nikolaeva et al., 2008). We distributed the particles and they are marked either chemical agent or not. This approach is known as “Marker-in-Cell Method” and well documented in, for example, Gerya (2010). The movements of particles were determined by

$$\frac{d\underline{r}}{dt} = \underline{v} + V_{\text{mig}} \underline{e}_z \quad (6)$$

where \underline{r} is the position vector of each particle and $V_{\text{mig}} \underline{e}_z$ is the migration velocity of chemical agent relative to the moving mantle. This velocity is equivalent to the “effective” hydration velocity of Gerya et al. (2002) and Gorczyk et al. (2007) and it is based on the idea that the water migration is controlled by the water supply from the slab (Peacock, 1990). In this study, we took this value as a parameter (see below). Initial number of the particles in each finite volume is 8 ($= 2^3$: for 3D) or 4 ($= 2^2$: for 2D) and we distributed them with small random displacements as described in Gerya and Yuen (2003b). The concentration of chemical agent in each finite volume was obtained by taking a weighted average of particles in each finite volume as described in Gerya and Yuen (2003b). We removed the particles below 160 km from the surface to avoid the artificiality produced near the left corner of Fig. 1. Since there is no kinematically

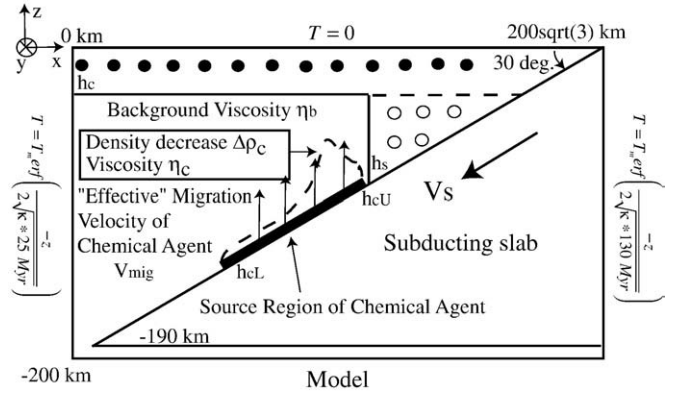


Fig. 1. A schematic view of the present model. Kinematically subducting slab (lower triangular region) with the speed V_s , the conductive layer on the top (black dotted region) and the non-moving mantle corner wedge (circle dotted region). The origin of coordinates is located at the top left corner. The modeled region covers $200\sqrt{3}$ km \times $200\sqrt{3}$ km \times 200 km. The detail will be described in the text.

moving slab, the entrainment of the particles becomes weak. This results in a rise of chemically buoyant plumes, when V_{mig} is small.

Physical properties of the mantle except the density and viscosity are assumed to be constant. The viscosity depends on the concentration of chemical agent as

$$\eta = \begin{cases} \eta_b & (c = 0) \\ R_\eta \eta_b & (c > 0) \end{cases} \quad (7)$$

where R_η is a constant and η_b is the background viscosity (see below). The meaning and the values of symbols are summarized in Table 1.

Fig. 1 shows a schematic cross section of the present model. For three-dimensional cases, this cross section extends toward y -direction. The region covers $200\sqrt{3}$ km \times $200\sqrt{3}$ km \times 200 km. The slab is represented by the lower triangular region which moves kinematically with the speed V_s shallower than 190 km. V_s is assumed to be 10 cm/year and the dip angle is set to 30° that roughly corresponds to the subduction of the Pacific plate under Northeast Japan. The place where the chemical agent emanates from the slab is shown by thick line on the top surface of slab. This region is

Table 1
Meaning of symbols.

Symbol	Meaning and value
c	Concentration of chemical agent
\underline{e}_z	Unit vector for z -direction. Positive upward
g	Gravity (10 m/s ²)
h_c h_s	See Fig. 1
h_{cL} h_{cU}	See Fig. 1
p	Pressure
R_η	Viscosity ratio ($= \eta_c / \eta_b$)
R_ρ	Density ratio ($= \Delta\rho_c / \rho_0 \alpha T_m$)
\underline{r}	Position vector of particle
T	Temperature
T_m	Mantle temperature (1300 °C)
t	Time
t_{plate}	Age of plate
$v(V_i)$	Velocity (velocity component of i -direction)
V_s	Speed of subduction (10 cm/year)
V_{mig}	Speed of migration of chemical agent
x, y, z	Cartesian coordinates. z is the vertical direction
α	Thermal expansivity (3×10^{-5} 1/K)
$\Delta\rho_c$	Density decrease associated with the chemical Pollution
η	Viscosity
η_b, η_c	Background viscosity, viscosity of polluted mantle
κ	Thermal diffusivity (10^{-6} m ² /s)
ρ, ρ_0	Density, reference density (3.3×10^3 kg/m ³)
$\underline{\tau}(\tau_{ij})$	Stress tensor (component)

characterized by the upper depth h_{cU} and the lower depth h_{cL} . We do not consider the along-arc variation of the source of the chemical agent for simplicity.

We assumed the existence of conducting (non-moving) region in the shallow part of the overlying plate (black dotted region in Fig. 1) and the corner of the mantle wedge (circular dotted region in Fig. 1). The geometry of this region is characterized by h_c and h_s . h_c is considered to be the bottom of the hard layer, i.e., the lithosphere and/or that of light layer, i.e., the crust. The viscosity of mantle wedge is η_b , the background viscosity, and it is constant for simplicity and ease of understanding the results. The chemical agent is characterized by the density difference $\Delta\rho_c$ and the viscosity η_c . We also use the ratio $R_\rho = \Delta\rho_c/\rho\alpha T_m$ (T_m is the mantle temperature) and $R_\eta = \eta_c/\eta_b$ to characterize the chemical anomaly.

The temperature boundary conditions at top and left/right sides are constant. They are given by:

Top surface:

$$T = 0 \quad (8)$$

Left and right sides:

$$T = T_m \operatorname{erf}\left(\frac{-z}{2\sqrt{\kappa t_{\text{plate}}}}\right) \quad (9)$$

where t_{plate} is either 25 Myr (left) or 130 Myr (right) mimicking the present subduction under the NE Japan. The boundary condition at the bottom is zero vertical gradient of the temperature. Since the advection of heat by the slab is large, this boundary condition hardly affects the temperature in the mantle wedge. The boundary conditions at front/back sides are reflective.

The flow boundary condition at the top surface is impermeable and free slip and that at the left is the same one as used before (Honda, 2009),

$$v_y = v_z = \frac{\partial p}{\partial x} = 0 \quad (10)$$

which allows the flow come in and come out. To check the effects of this boundary condition, we calculated the 2D case with twice the horizontal size. We found that, although the precise value is different, the overall character such as the flow pattern and temporal variation of the flow is similar. The flow boundary condition at the bottom is permeable, that is,

$$v_x = v_y = -p + \frac{\partial v_z}{\partial z} = 0 \quad (11)$$

The flow boundary conditions at front/back sides are impermeable and reflective.

The initial temperature field for most of the models except Case 11 was calculated without the chemical agent. The start-up temperature for obtaining the initial condition was uniform temperature given by (9) with $t_{\text{plate}} = 25$ Myr. Then, we started the kinematic movement of subducting slab. The temperature in the non-moving mantle wedge changes most slowly, since the conduction is only the mechanism of heat transfer there. We used the solution at 15.5 Myr after the start of the calculation. Using this solution as an initial condition, we introduced the chemical agent corresponding to each case.

The basic equations were discretized by the uniform finite volumes ($128 \times 128 \times 128$; aspect ratio $\sqrt{3}:\sqrt{3}:1$) and solved by the code modified from “stag3d” (Tackley, 1993). Particle tracking was done using the 4th order Runge–Kutta method. The time stepping is 0.5 Courant time step which usually gives a well-resolved results with time. The resolution test was done using 2D model with 128×128 and 256×256 finite volumes for 2D equivalent model of Case 12 in Table 2. We found a good agreement, if the chemical agent is not included (see

Table 2
Cases studied.

Case	h_c (km)	h_s (km)	h_{cU} (km)	h_{cL} (km)	η_b (Pa s)	R_η	R_ρ	V_{mig} (cm/year)
1	30	90	90	150	4×10^{20}	0.01	0	10
2	30	90	90	150	4×10^{20}	0.01	0.15	10
3	30	90	90	150	4×10^{20}	0.01	0.5	10
4 ^a	30	90	90	150	4×10^{20}	0.01	1	10
5 ^b	30	90	90	150	4×10^{20}	0.01	1	1
6	30	90	90	150	4×10^{19}	0.1	1	1
7	30	90	90	150	1×10^{19}	0.04	1	1
8	30	90	90	150	4×10^{20}	0.01	1	10
9	30	90	90	150	4×10^{19}	0.1	1	10
10	30	90	90	150	1×10^{19}	0.04	1	10
11 ^d	30	30	30	150	4×10^{20}	0.1, 0.0025	1, 0	10
12 ^{e,c}	30	90	90	150	4×10^{20}	0.01	0	N/A
13 ^f	46	90	90	150	4×10^{20}	0.0025	0	N/A
14 ^g	50	90	90	150	4×10^{20}	0.0025	0	N/A

^a 2D model was used for test of particle density. Fig. 2C and D.

^b 2D model was used for test of particle density. Fig. 2E and F.

^c 2D model was used for test of mesh resolution. Fig. 2A and B.

^d Case with no rigid corner. The first and the second values of R_η and R_ρ are for the upper and lower part, respectively. This boundary is located at 90 km.

^e The LVW is fixed in space.

^f The LVW is fixed in space.

^g The LVW is fixed in space.

A and B of Fig. 2). To check the effects of density of particles, we tested 2D cases with 4 and 16 particles per finite volume for 128×128 finite volumes (2D equivalent models of Cases 5 and 12 in Table 1). We found that, if V_{mig} is large ($=10$ cm/year: Case 5), the agreement between two cases is very good (see C and D of Fig. 2). If V_{mig} is small (i.e., $=1$ cm/year: Case 12), we found significant differences (see E and F of Fig. 2). There are many “holes” in the concentration field of chemical agent meaning that no particles exist in a corresponding finite volume. However, since the qualitative behavior of the system is similar between these 4 and 16 particles cases and we mainly use the results with $V_{\text{mig}} = 10$ cm/year in the following discussions, we believe that the conclusions presented here will not be affected by further improvements of numerical method. Further increase of the number of particles in 3D cases encounters serious computational inconvenience by the present algorithm.

3. Results

Although our model is simple, we still need lots of free parameters specified. All the cases presented in this paper are summarized in Table 2 along with important parameters.

We set $h_c = 30$ km, $h_s = 90$ km, $h_{cU} = 90$ km and $h_{cL} = 150$ km for most of the models. For several cases, which are mentioned explicitly, we used the different values. Those values were chosen based on arguments of the non-moving mantle wedge, or “nose” and the depth of the dehydration (Honda, 1985; Iwamori, 1998; Kneller et al., 2005; Conder, 2005). The typical value of the background viscosity is selected to be 4×10^{20} Pa s and that of the chemical anomaly is 4×10^{18} Pa s, that is, $R_\eta = 0.01$. If V_{mig} is large, we expect the existence of almost time-independent distribution of the low viscosity wedge (LVW: Billen and Gurnis, 2001), associated with the concentration of chemical agent, similar to that of previous models (e.g., Honda and Yoshida (2005); see Fig. 2C and D). Thus, the thermal buoyancy may play an important role in this case. On the contrary, if V_{mig} is small, the behavior of the chemical anomaly may dominate the system. Considering these, we chose $V_{\text{mig}} = 10$ cm/year and 1 cm/year as representative values of the former and latter cases, respectively. The density anomaly caused by the chemical agent is set mainly $R_\rho = 0$ or 1 as the representatives of the pure thermal and chemical density dominated convection. The reference case has $\eta_b = 4 \times 10^{20}$ Pa s and $R_\eta = 0.01$, that is, $\eta_c = 4 \times 10^{18}$ Pa s (Case 1 of Table 2).

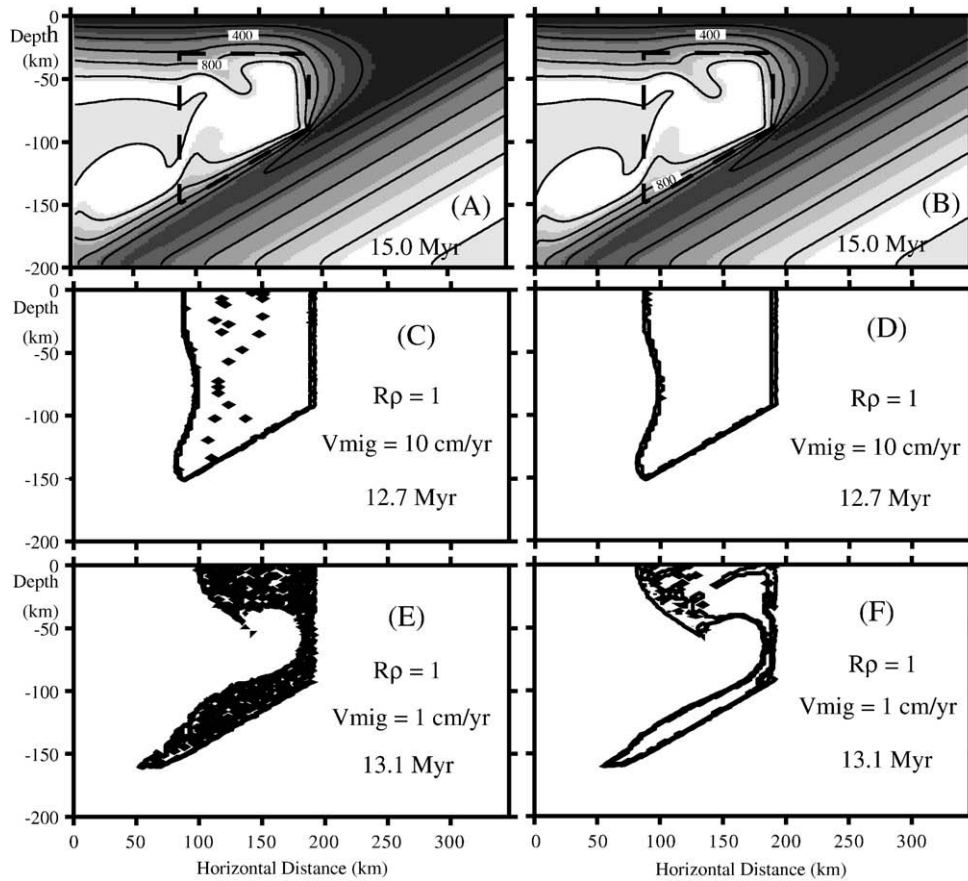


Fig. 2. Test of resolution and number of particles. The temperature field of 2D equivalent model of Case 12 in Table 2 for 128×128 (A) and 256×256 (B) finite volumes. The interval of contour is 200° . Numbers in A and B show the temperatures in $^\circ\text{C}$. The region enclosed by dashed lines is the low viscosity wedge (LVW). The concentration of chemical agent c of 2D equivalent model of Case 4 for 4 particles (C) and 16 particles (D). The contour is drawn for 0.5 and 1. The concentration of chemical agent of 2D equivalent model of Case 5 for 4 particles (E) and 16 particles (F). The time in the figure is the time after the introduction of chemical agent.

Fig. 3a shows the variation of pattern of small-scale convection with regard to the increase of R_p for the reference case with $V_{\text{mig}} = 10$ cm/year. The time in the figures shows the time elapsed after the introduction of chemical agent. The case with $R_p = 0$ is the purely thermal convection and it is almost equivalent to the previous models (e.g., Honda and Yoshida, 2005). Since the migration velocity of the chemical anomaly is large, the three-dimensional distribution of chemical anomaly, i.e., LVW is similar to the one as assumed by previous works (see Fig. 2C and D). For this case, we also confirmed that the small-scale convection occurs in the mantle wedge whose viscosity is around 10^{18} Pa s. The difference between the present and the previous models can be seen in the temporal behavior of the convection pattern. We found that the pattern of small-scale convection is stable with time and it does not show the “flip-flop” pattern, that is, the previous hot region becomes cold one and vice versa, as reported in the previous work (Honda and Yoshida, 2005). We return this point later.

As the contribution of chemical agent, i.e. R_p increases, the convection pattern loses its three-dimensional character and it becomes two-dimensional. As R_p increases, the flow close to the forearc region is dominated by the chemical density anomaly. Since the chemical anomaly has a low density, the region polluted by chemical agent tends to stay (stagnate) in the corner of the mantle wedge (it cannot be recycled by the other part of the mantle). As a result, the temperature there becomes low as a whole (hot material is not carried toward this region) and this suppresses the occurrence of thermal instability.

Fig. 3b shows the vertical cross sections of flow velocity, temperature and the concentration of the chemical agent at

$y = 172$ km for $R_p = 0$ (left figure: (A) of Fig. 3a) and $R_p = 1$ (right figure: (D) of Fig. 3a). For $R_p = 0$, the mantle in the polluted area (shown by white) is dragged into the deep mantle, and it follows the emplacement of hotter mantle. Meanwhile, for $R_p = 1$, the circulation occurs in the polluted area implying no replacement by the hotter mantle. If the along-arc variation of the source of the chemical agent exists, we may expect the 3D flow in the polluted mantle. However, this point is outside the scope of the present study.

We conducted simulations with $V_{\text{mig}} = 1$ cm/year. Fig. 4a shows the pattern changes with the decrease of the background viscosity η_b from that of reference case ((A): $\eta_b = 4 \times 10^{20}$ Pa s), by one-tenth ((B): $\eta_b = 4 \times 10^{19}$) and by fortieth ((C): $\eta_b = 1 \times 10^{19}$ Pa s). R_p is kept constant and η_c is 4×10^{18} Pa s except (C) in which we used $\eta_c = 4 \times 10^{17}$ Pa s. From this figure, we recognized the emergence of 3D structure with the decrease of the background viscosity. The absolute value of η_b which determines the behavior of the chemical plumes depends on other factor such as the velocity of subduction. This topic is outside the scope of the present work.

With the same parameters as those given in the above cases, we increased $V_{\text{mig}} = 10$ cm/year (Fig. 4b). All the temperature fields become almost two-dimensional. Only for the cases with the lowest η_b and η_c , i.e., (C), overlapping the large scale 2D thermal structure, we see the small-scale 3D structure. Although these results depend on other parameters such as V_s and V_{mig} , the suppression of the 3D instability by the chemical density difference is evident.

From these results, we see the polluted mantle tends to stay in the mantle wedge. As a result, it becomes cold, since it is not replaced by the hot mantle. Thus, this may suggest the chemical origin of cold mantle wedge or “nose” (e.g., Honda, 1985; Kneller et al., 2005; Wada

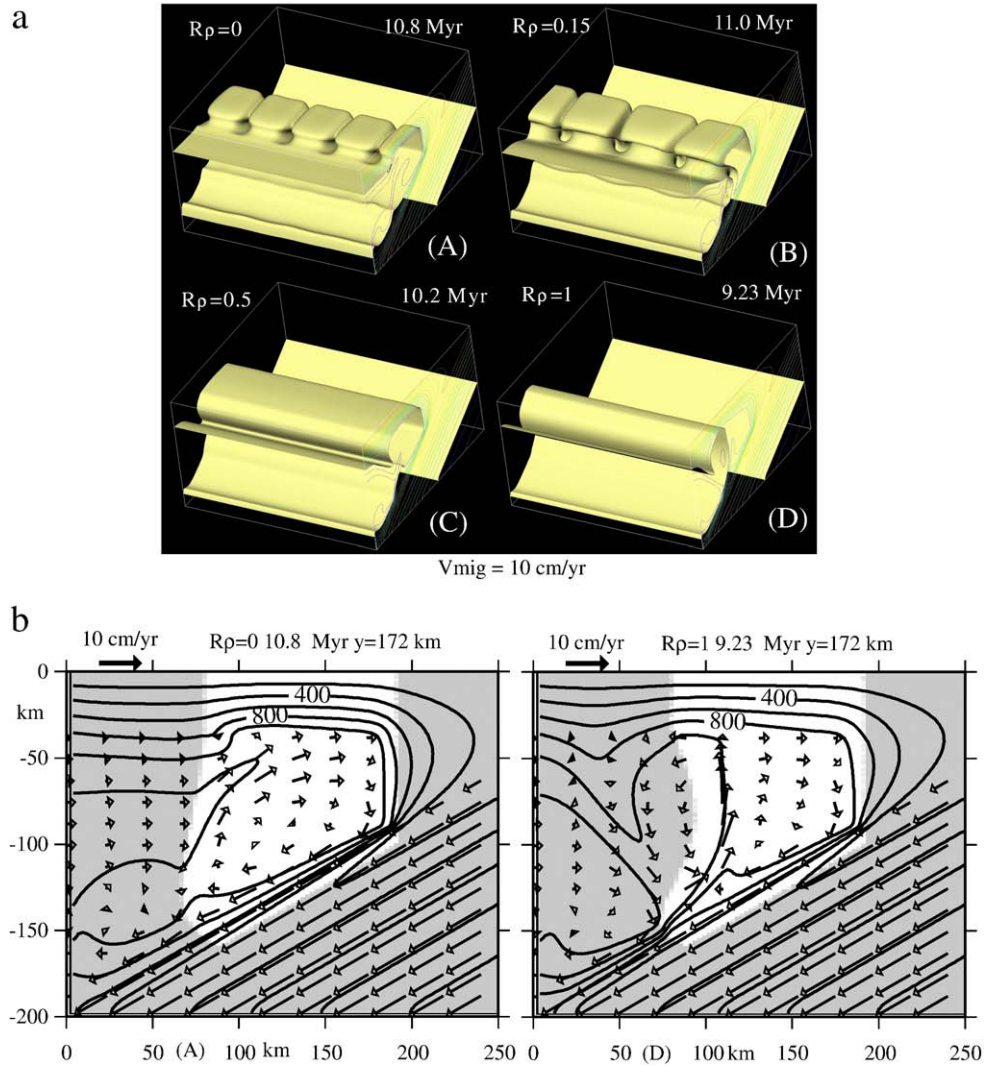


Fig. 3. (a) The 3D temperature field of Cases 1 (A), 2 (B), 3 (C) and 4 (D). The value of isothermal surface is 1000 °C. Thin contours on the right walls are the temperatures drawn by every 200°. The time in the figure is the time after the introduction of chemical agent. The modeled region covers $200\sqrt{3} \text{ km} \times 200\sqrt{3} \text{ km} \times 200 \text{ km}$. As R_ρ increases, 3D thermal structure becomes 2D. (b) Vertical cross sections of (A) and (D) of Fig. 3a at $y=172 \text{ km}$. The arrow shows the velocity vector projected on the cross sections. Its scale is shown on the left corner of the figure. The thick contours show the temperature distribution and their interval is 200°. White zone shows $c=1$, that is, the chemically polluted mantle. Note the circulation in the polluted mantle for (D) (right figure).

et al., 2008). To see this, we undertook the studies of other type of models in which the chemical agent acts on the density and viscosity at shallower depth and it acts only on the viscosity at deeper depth.

Fig. 5 is an example of such models. In this model, there is no conductive corner (circular dotted region in Fig. 1, that is, $h_c = 30 \text{ km}$) and we set $h_{cU} = 30 \text{ km}$ and $h_{cL} = 150 \text{ km}$. The initial temperature is the uniform temperature given by (4) with $t_{age} = 25 \text{ Myr}$. The chemical agent emanating from 30 km to 90 km decreases the viscosity by the factor of 0.1 ($\eta_c = 4 \times 10^{19} \text{ Pa s}$) and the density decrease characterized by $R_\rho = 1$, while it emanating from 90 to 150 km only reduces the viscosity by 0.0025 ($\eta = 1 \times 10^{18} \text{ Pa s}$). This case approximates the situation in which the major dehydration generally occurs at shallow depth and/or the capability of absorbing the water in the mineral is generally large in the shallow depth and it is small in the mantle wedge (see, for example, the results of Iwamori (1998) and Arcay et al. (2005)). A large amount of water may affect both the density and the viscosity, while the small amount of water may only affect the viscosity. Larger R_η under the forearc mimics the higher viscosity there caused by its temperature dependence.

The model shows a low temperature corner wedge despite the full coupling between the mantle wedge and the subducting slab, and the

small-scale convection in the back arc. For the 3D small-scale convection to occur, the model requires lower viscosity (from 4×10^{18} to 1×10^{18} : See Table 2) than that required for the model with artificially imposed non-moving wedge corner (Fig. 3 (A)). This is consistent with the previous result, that is, the low chemical anomaly tends to suppress the 3D thermal instability.

As noted before, we found that the temporal evolution of small-scale convection is fairly stable, that is, it does not show the flip-flop type of temporal evolution, while our previous study (Honda and Yoshida, 2005) does. To understand this discrepancy, we studied several cases using the model similar to the previous studies (Honda and Yoshida, 2005). In this model, the time-independent shape of the low viscosity mantle wedge (LVW) is trapezoidal whose side vertical walls are the plane defined by $h_{cU} = 90 \text{ km}$ and $h_{cL} = 150 \text{ km}$ and the front and back vertical boundaries (see Fig. 1). The top horizontal plane is defined by h_c and the bottom plane is the top of the slab. The background viscosity η_b is $4 \times 10^{20} \text{ Pa s}$. Both h_c and η_c were changed as described below. The models do not include the chemical density anomaly.

The results are summarized in Fig. 6a. (A) of Fig. 6a ($h_c = 30 \text{ km}$ and $\eta_c = 4 \times 10^{18} \text{ Pa s}$ with fixed geometry of LVW) shows the stability

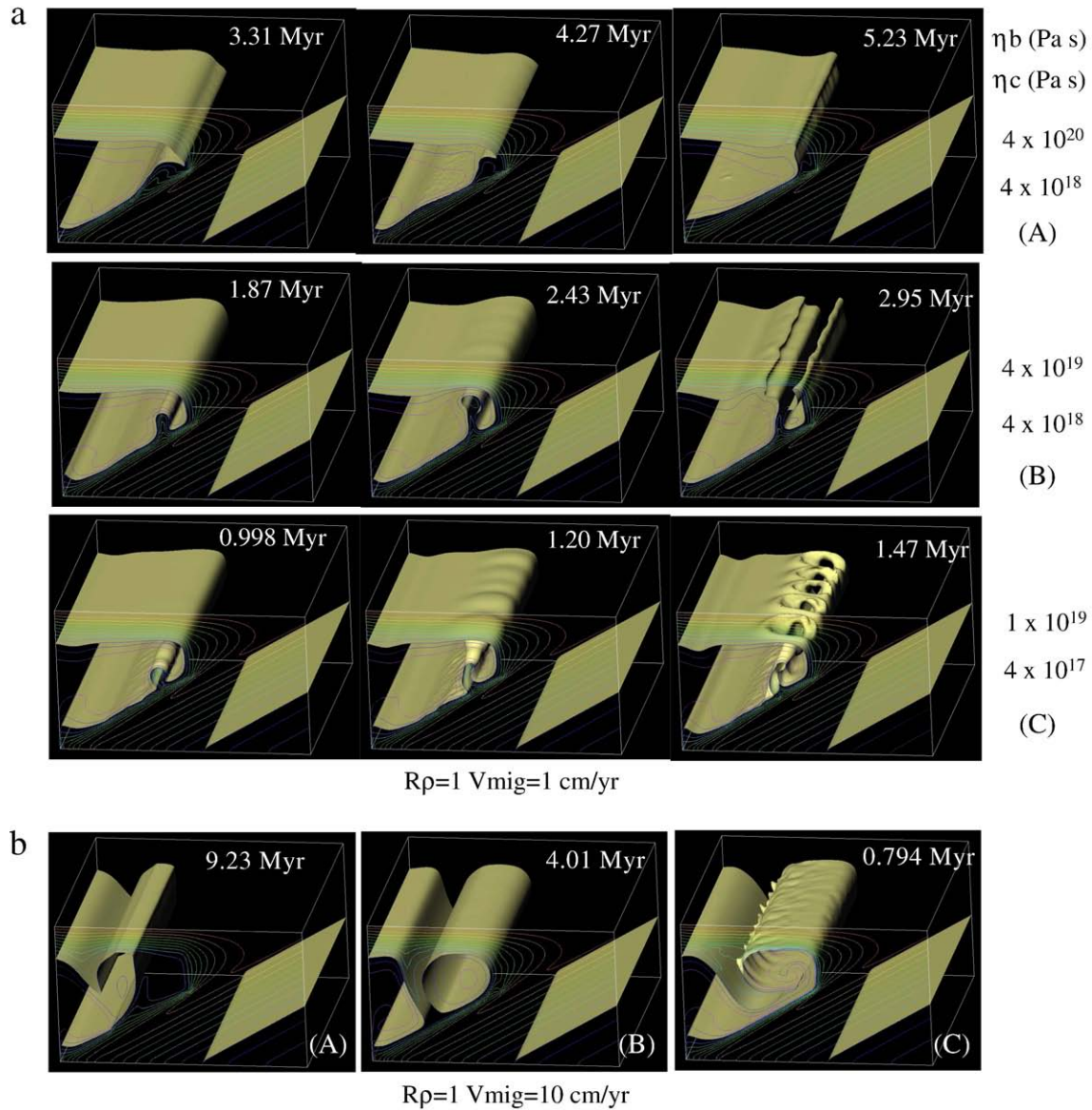


Fig. 4. (a) The 3D temperature field of Cases 5 (A), 6 (B) and 7 (C). The value of isothermal surface is 1000 °C. Thin contours on the front wall show the temperatures drawn by every 200°. The time in the figure is the time after the introduction of chemical agent. The modeled region covers $200\sqrt{3}$ km \times $200\sqrt{3}$ km \times 200 km. The background viscosity η_b and the viscosity of polluted mantle η_c are given in the left of figures. (b) The 3D temperature field of Cases 8 (A), 9 (B) and 10 (C). All the parameters except V_{mig} is the same as corresponding cases shown in Fig. 4a of A, B and C. The value of isothermal surface is 1000 °C. Thin contours on the right walls show the temperatures drawn by every 200°. The time in the figure is the time after the introduction of chemical agent. The modeled region covers $200\sqrt{3}$ km \times $200\sqrt{3}$ km \times 200 km. The 3D thermal structure observed with $V_{mig} = 1$ cm/year (Fig. 4a) almost disappears with $V_{mig} = 10$ cm/year.

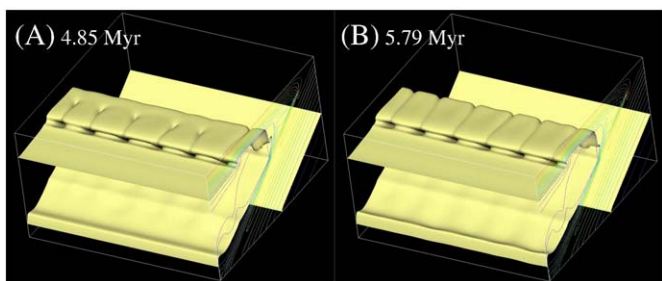


Fig. 5. The 3D temperature field of Case 11 (no corner edge) in Table 2. The value of isothermal surface is 1000 °C. Thin contours on the right walls show the temperatures drawn by every 200°. The time in the figure is the time after the introduction of chemical agent. The modeled region covers $200\sqrt{3}$ km \times $200\sqrt{3}$ km \times 200 km. In this case, there is no rigid corner region (circle dotted region of Fig. 1), that is, $h_s = h_c = 30$ km.

of the pattern of the small-scale convection. However, as h_c increases, the pattern of small-scale convection changes its temporal behavior. (B) ($h_c = 46$ km, $\eta_c = 1 \times 10^{18}$ Pa s with fixed LVW) shows a flip-flop pattern, that is, the previous hot region becomes cold one and vice versa.

h_c controls the thickness of the available cold boundary layer under the back-arc side of the plate. If it is thick, the cold material needed for the formation of small-scale downgoing flow is supplied in situ. As the thermal boundary layer becomes thin because of the increase of h_c , the cold material should be supplied from the other part, also. This will affect the neighboring flow.

Fig. 6b shows horizontal flow patterns at 32.0 km (top) and 49.2 km (bottom), just below the conductive lid, for (A) ($h_c = 30$ km) and (B) ($h_c = 50$ km) of Fig. 6a. While the case with thinner h_c (top) shows a stable flow pattern, the case with thicker h_c (bottom) shows a significant interaction between plumes near their back-arc end.

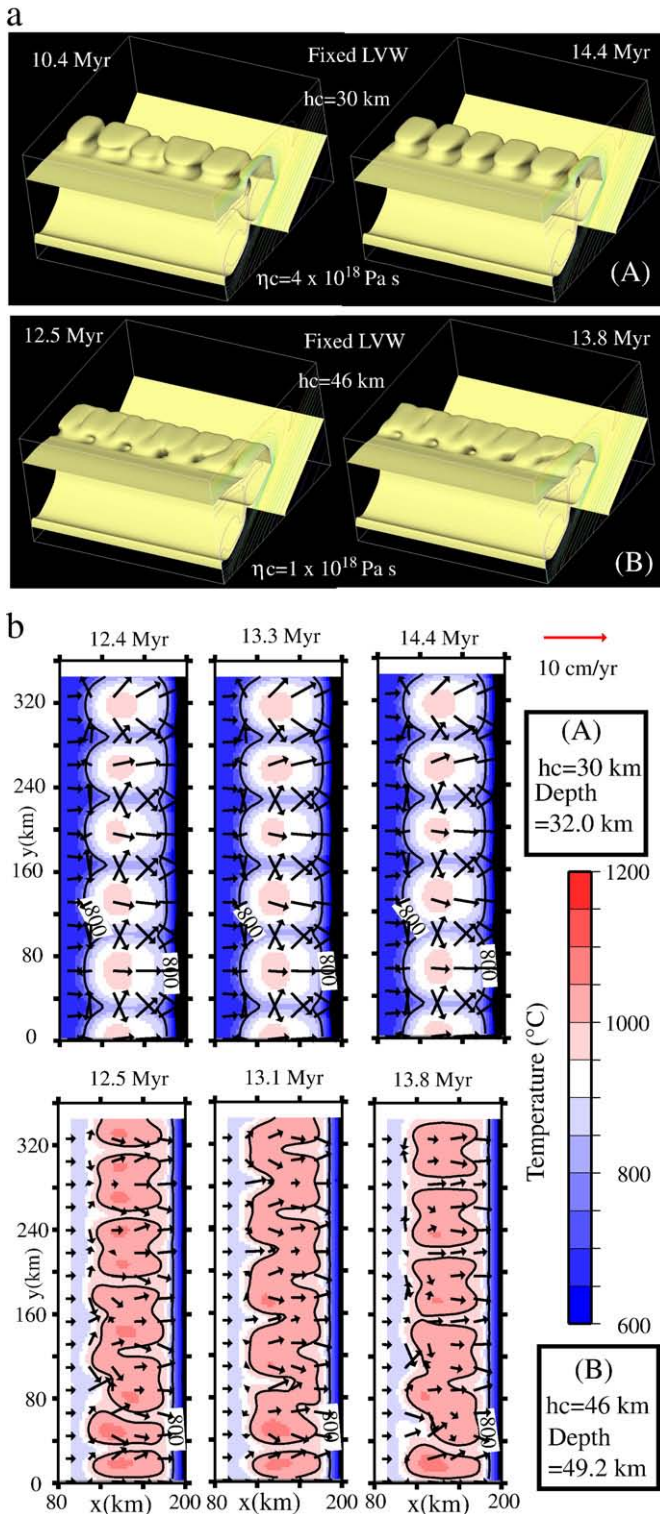


Fig. 6. (a) The 3D temperature field of Case 12 (A) and Case 13 (B). The value of isothermal surface is 1000 °C. Thin contours on the right walls show the temperatures drawn by every 200°. The time in the figure is the time after the introduction of chemical agent. The modeled region covers $200\sqrt{3} \text{ km} \times 200\sqrt{3} \text{ km} \times 200 \text{ km}$. The low viscosity wedge (LVW) is fixed in space. As h_c increases, the spatial pattern of the small-scale convection changes from steady one to flip-flop pattern, that is, the hot region becomes cold one and vice versa. (b) Temporal and spatial changes of horizontal velocity and temperature for A and B of Fig. 6a. Arrow shows the horizontal velocity and its scale is shown on the right corner of the figure. The contour and the gray scale (color version is available on the website) show the temperature field. The contour interval is 200°. Numbers in the figures are the temperatures in °C.

We also note here that the increase of h_c requires lowering of η_c , since the 3D small-scale convection becomes suppressed. Further increase of h_c will result in the cessation of small-scale convection, since the cold material to drive the flow is no longer available.

As explained before, h_c is considered to be the bottom of the lithosphere and/or the crust. For the former case, we may expect a relation between h_c and the thickness of the thermal boundary layer through the temperature-dependent viscosity. On the contrary, for the latter case, we may not have a direct relation. Although we tried to construct a general model as possible as we can, the model, especially the geometry is tuned to the subduction zone in the NE Honshu, Japan which was investigated by us. Since the present crustal thickness there is about 30 km, we mainly focus on $h_c = 30 \text{ km}$. It may be interesting to study the relation between h_c and the pattern of the small-scale convection systematically for the case without the crust.

4. Discussions

The important parameters of this study are the viscosity and the density difference caused by the chemistry. Recent review of rheological properties of olivine was done by Karato (2010). Based on his estimates, the viscosity of wet olivine around 10^{18} Pa s may be possible (see Figure 9 of Karato (2010)). A simple estimate shows that the density difference caused by an inclusion of a few percent water becomes comparable to that caused by the thermal expansion (implying $R_\rho \sim 1$). Thus, the models are realistic in this sense.

In the following, we will discuss the geologically important topics (1) the formation of cold “nose” and the small-scale convection whose pattern may be reflected in that of volcano distribution.

The presence of non-moving mantle corner wedge was suggested by many workers (e.g., Honda, 1985; Kneller et al., 2005; Conder, 2005; Wada et al., 2008) based on the comparison of heat flow distribution in the forearc and that obtained by the numerical models. The reasoning is quite simple. If the mantle flow reaches the corner of the mantle wedge, the heat flow of the forearc becomes too high. This suggests some kind of decoupling between the shallow part of the mantle wedge and the subducting plate. Honda (1985) presumed that the occurrence of thrust type earthquakes at shallow depth was an evidence of such a decoupling. He suggested that the aseismic front (Yoshii, 1975, 1979), whose cross line on the top surface of the subducting slab roughly corresponds to the deepest limit of the thrust zone ($\approx 60 \text{ km}$), is the back-arc limit of such a non-moving mantle wedge. However, actually, his best model suggests that its boundary is further away toward the back arc. Later study using more complicated and realistic rheology by Kneller et al. (2005) proposed a decoupling and partial decoupling up to 70 km depth. Thus, these results suggest that some kind of decoupling exists further down the region where the thrust type earthquakes occur. Our model suggests that even when the coupling between the mantle wedge and the subducting slab occurs, the chemical buoyancy can explain the low temperature regime. It is worth noting that the more realistic models in the line of our modeling approach have shown such features (Gorczyk et al., 2006; Nikolaeva et al., 2008), also. Thus, our results may suggest the importance of considering the chemical effects to understand the dynamics of the corner of the mantle wedge. We do not mean that “only” the chemical density difference is the cause of cold nose. The previous works as cited above and recent elaborate study by Wada et al. (2008) assumed or showed that the mechanical decoupling also plays an important role on the formation of cold nose.

As we have shown that the flip-flop nature of small-scale convection depends on the thickness of the thermal boundary layer under the back arc. As the thickness increases, the pattern of convection becomes stabilized. In the model of Honda and Yoshida (2005), they assumed a uniform high mantle temperature as the initial condition to mimic the back-arc opening of Japan Sea. As a result, the thermal boundary layer under the back arc gradually

increases over time. Thus, when the small-scale convection starts to occur, the thermal boundary layer is thin. This will result in the flip-flop pattern of temporal change. From this result, [Honda and Yoshida \(2005\)](#) pointed out that the past distribution of volcanoes in the NE Honshu may suggest such a flip-flop pattern for the validation of their model.

We note that the interpretation of past volcano distribution in the NE Honshu also allows the alternative view that the pattern was stable and the roll pattern gradually appeared as the small-scale convection became vigorous. This is because we do not know the age distribution under the presently active area.

Other important point which [Honda and Yoshida \(2005\)](#) suggested is the migration of volcanic activity from the back arc to the trench, which is also observed in Izu–Bonin subduction zone (e.g., [Honda et al., 2007](#)). This might not be able to be explained by the stable pattern of convection and may involve more complex non-steady thermal (e.g. [Fig. 6b](#)) and thermal–chemical (e.g. [Fig. 4a](#)) plumes.

5. Conclusions

In this study, we have developed a simple model of small-scale convection in the mantle wedge driven both by thermal and chemical density anomalies. Our major finding is that the chemically buoyant material suppresses the three-dimensional instability caused by the thermal effects, when the along-arc variation of chemical source does not exist. Our results suggest the importance of chemical density for the origin of cold mantle wedge or nose in the corner of the mantle wedge. We also studied the temporal variation of three-dimensional pattern of small-scale convection and found that the thickness of the thermal boundary layer under the back arc controls it. The thick thermal boundary layer tends to suppress the temporal pattern change and the thin boundary layer makes the flow flip-flop type ([Honda and Yoshida, 2005](#)). Present results will provide the basis for understanding the origin and temporal evolution of island arc volcanism.

Acknowledgements

We thank three anonymous reviewers for their comments which improve the manuscript significantly. Also, we thank Yanick Ricard for his quick handling of paper and suggestions. This work was supported by the Grant-in-Aid for Science Research in the Priority Areas of “Stagnant Slab: A keyword to Mantle Dynamics” (16075208) and SNF Research 200021-11638/1. Computations were done at the Earthquake Information Center, Earthquake Research Institute, University of Tokyo. The Generic Mapping Tools ([Wessel and Smith, 1998](#)) were used for drawing some figures.

References

Arcay, D., Tric, E., Doin, M.P., 2005. Numerical simulations of subduction zones: effect of slab dehydration on the mantle wedge dynamics. *Phys. Earth Planet. Int.* 149, 133–153.

- Billen, M., Gurnis, M., 2001. A low viscosity wedge in subduction zones. *Earth Planet. Sci. Lett.* 193, 227–236.
- Conder, J.A., 2005. A case for hot slab surface temperatures in numerical viscous flow models of subduction zones with an improved fault zone parameterization. *Phys. Earth Planet. Int.* 149, 155–164.
- Gerya, T., 2010. *Introduction to Numerical Geodynamic Modelling*. Cambridge University Press. 344 pp.
- Gerya, T., Yuen, D.A., 2003a. Rayleigh–Taylor instabilities from hydration and melting propel ‘cold plumes’ at subduction zones. *Earth Planet. Sci. Lett.* 212, 47–62.
- Gerya, T., Yuen, D.A., 2003b. Characteristics-based marker-in-cell method with conservative finite-differences schemes for modeling geological flows with strongly variable transport properties. *Phys. Earth Planet. Int.* 140, 293–318.
- Gerya, T.V., Stoeckert, B., Perchuk, A.L., 2002. Exhumation of high-pressure metamorphic rocks in a subduction channel – a numerical simulation. *Tectonics* 21 (6) 6–19.
- Gerya, T.V., Yuen, D.A., Sevre, E.O.D., 2004. Dynamical causes for incipient magma chambers above slabs. *Geology* 32, 80–92.
- Gerya, T.V., Connolly, J.A.D., Yuen, D.A., Górczyk, W., Capel, A.M., 2006. Seismic implications of mantle wedge plumes. *Phys. Earth Planet. Int.* 156, 59–74.
- Górczyk, W., Gerya, T.V., Connolly, J.A.D., Yuen, D.A., Rudolph, M., 2006. Large-scale rigid-body rotation in the mantle wedge and its implications for seismic tomography. *Geochem. Geophys. Geosyst.* 7. doi:10.1029/2005GC001075.
- Górczyk, W., Willner, A.P., Gerya, T.V., Connolly, J.A.D., Burg, J.-P., 2007. Physical controls of magmatic productivity at Pacific-type convergent margins: new insights from numerical modeling. *Phys. Earth Planet. Int.* 163, 209–232.
- Hasebe, K., Fujii, N., Uyeda, S., 1970. Thermal processes under island arcs. *Tectonophysics* 10, 335–355.
- Honda, S., 1985. Thermal structure beneath Tohoku, Northeast Japan – a case study for understanding the detailed thermal structure of the subduction zone. *Tectonophysics* 112, 69–102.
- Honda, S., 2009. Numerical simulations of mantle flow around slab edges. *Earth Planet. Sci. Lett.* 277, 112–122.
- Honda, S., Yoshida, T., 2005. Application of the model of small-scale convection under the island arc to the NE Honshu subduction zone. *Geochem. Geophys. Geosyst.* v6, Q01002. doi:10.1029/2004GC000785.
- Honda, S., Yoshida, T., Aoike, K., 2007. Spatial and temporal evolution of arc volcanism in the northeast Honshu and Izu–Bonin arcs: evidence of small-scale convection under the island arc? *Island Arc* 16, 214–223.
- Iwamori, H., 1998. Transportation of H₂O and melting in subduction zones. *Earth Planet. Sci. Lett.* 160, 65–80.
- Karato, S., 2010. Rheology of the deep upper mantle and its implications for the preservation of the continental roots: a review. *Tectonophysics* 481, 82–98.
- Karato, S., Wu, P., 2003. Rheology of the upper mantle: a synthesis. *Science* 260, 771–778.
- Kneller, E.A., van Keken, P.E., Karato, S., Park, J., 2005. B-type olivine fabric in the mantle wedge: insights from high-resolution non-Newtonian subduction zone models. *Earth Planet. Sci. Lett.* 237, 781–797.
- Nikolaeva, K., Gerya, T.V., Connolly, J.A.D., 2008. Numerical modelling of crustal growth in intraoceanic volcanic arcs. *Phys. Earth Planet. Int.* 171, 336–356.
- Peacock, S.M., 1990. Fluid processes in subduction zones. *Science* 248, 329–337.
- Poli, S., Schmidt, M.W., 2002. Petrology of subducted slabs. *Annu. Rev. Earth Planet. Sci.* 30, 207–235.
- Tackley, P.J., 1993. Effects of strongly temperature-dependent viscosity on time-dependent, three-dimensional models of mantle convection. *Geophys. Res. Lett.* 20, 2187–2190.
- Toksoz, M.N., Minear, J.W., Julian, B.R., 1971. Temperature field and geophysical effects of a downgoing slab. *J. Geophys. Res.* 76, 177–196.
- Wada, I., Wang, K., He, J., Hyndman, R.D., 2008. Weakening of the subduction interface and its effects on surface heat flow, slab dehydration, and mantle wedge serpentinization. *J. Geophys. Res.* 113, B04402. doi:10.1029/2007JB005190.
- Wessel, P., Smith, W.H.F., 1998. New improved version of the Generic Mapping Tools released. *EOS, Trans. AGU* 79 (47), 579.
- Yoshii, T., 1975. Proposal of the “aseismic front”. *Zisin* 2 (28), 365–367 (in Japanese).
- Yoshii, T., 1979. A detailed cross-section of the deep seismic zone beneath northeastern Honshu, Japan. *Tectonophysics* 55, 349–360.
- Zhu, G., Gerya, T.V., Yuen, D.A., Honda, S., Yoshida, T., Connolly, J.A.D., 2009. Three-dimensional dynamics of hydrous thermal-chemical plumes in oceanic subduction zones. *Geochem. Geophys. Geosyst.* 10. doi:10.1029/2009GC002625.